Visualizing Blood Flow Patterns Using Streamlines, Arrows, and Particle Paths

Michael H. Buonocore

A customized computer program (MRIView) is described for visualizing and quantifying complex blood flow patterns in major vessels, using nongated and cardiac-gated three-dimensional (3D) velocity data obtained with MR velocity-encoded phase pulse sequences. Streamlines, arrows, and particle paths (collectively referred to as "paths") can be computed interactively, using both forward and backward time integration of the velocity field. The program provides interactive cross-sectional and 3D perspective visualization of the paths, with quantification and statistical analysis of average speed, through-plane velocity, cross-sectional area, and flow. Normal flow patterns in the carotid artery, basilar artery tip, ascending aorta, coronary arteries, descending aorta, and renal arteries, as well as abnormal flow patterns in basilar tip aneurysms, have been investigated. The program revealed flow patterns in these regions with features that are well known from Doppler ultrasound and other features that have not been reported previously. The association between specific abnormal flow patterns and development of atherosclerosis suggests that particle paths can be used to assess risk of plaque formation and progression, as well as to evaluate flow dynamics and vascular patency before and after vascular interventions.
Key words: MRI; velocity-encoded phase imaging; flow visualization; image processing.

INTRODUCTION

The traditional cross-sectional display of independent velocity components can be improved to enable the user to more quickly and effectively see the content of velocity-encoded images obtained using MRI. Streamline visualization of the velocity field was first used with nongated three-dimensional (3D) phase-contrast angiography in the internal carotid artery and intracranial aneurysms, to show average flow trajectories and filling-time relationships (1). A later paper (2) described background, divergence, and local boundary correction algorithms that made the nongated experimental velocity data more consistent with the laws of fluid mechanics and improved streamline realism. So-called "arrow maps" were first used with MR cardiac-gated two-dimensional (2D) phase-contrast angiography (3) for visualization of ascending aorta flow in normal subjects (4), in patients

with central vessel aneurysms and grafts (5), and in patients with ischemic heart disease (6). They were composed of the velocity vectors or short-duration particle paths (i.e., arrows) displayed at every point on a uniform spatial grid within the vessel. Arrow maps were unique in revealing snapshots of the spatial organization of flow within the entire flow field.

A computer program, called MRIView, and requisite MR pulse sequences have been used to noninvasively visualize *in vivo* blood flow patterns using streamlines, arrows, and particle paths. The term "flow pattern" refers to a trajectory of blood movement through the vessel, that represents an appreciable fraction of the total blood volume, that exists for a measurable time interval and with measurable spatial extent and that may evolve into another pattern during the cardiac cycle or be sustained over the entire cardiac cycle. The program has been tested and refined using velocity data from standard velocity-encoded phase pulse sequences, in a variety of vascular regions (7–12). This is the first study to present flow patterns derived from 3D time-resolved (i.e., cardiac-gated) velocity data sets. The use of cardiac-gated data gives rise to the distinction between a streamline and a particle path. The term "streamline" refers to a path that is everywhere tangent to the velocity vectors at *a particular point in time*. It is the path that a particle would take if released into the velocity field with the field held constant. However, this path would not match the true path of the particle through the vessel, because velocity fields in vessels are, in fact, time-varying. A true particle path would be everywhere tangent to the velocity vectors at *different* points in time, so the definition of streamline would not be satisfied. When the velocity field is truly time-independent, the definitions of particle path and streamline are identical. Of course, nongated acquisitions provide a temporal pseudo-average of the actual time-varying velocity field, and streamlines derived from that velocity field should not be considered true particle paths. Of the three terms, "particle paths" is the inclusive term and will be used whenever the discussion applies to all.

METHODS

Pulse Sequences

Between October 25, 1993 and November 21, 1994, flow patterns in 20 normal subjects and three patients were evaluated in the following vascular regions: basilar artery and branches, one normal and three patients; carotid artery bifurcations, four normal subjects; descending aorta and renal arteries, four normal subjects; ascending aorta and left coronary arteries, 11 normal subjects. All subjects and patients gave informed consent. All studies were performed on a 1.5-T GE Signa Advantage MRI

system (General Electric Medical Systems, Milwaukee, WI) with scan parameters shown in Table 1. All nongated studies used 3D acquisition with four-point (x, y, z, baseline), three-direction velocity encoding (13). All cardiac-gated studies used 2D single-slice acquisition with the same velocity-encoding scheme, with multiple overlapping slice locations acquired one after the other (sequentially). Cardiac-gated velocity data were acquired asynchronously (without ECG triggering), and images were reconstructed retrospectively at equally spaced time points (frames) across the average RR interval and labeled by either a "frame number" (from 1 to the total number of frames), or by the "frame time" in seconds equal to ((frame no. − 1)/(total no. of frames)) × (RR interval). To determine the actual time of data acquisition after the ECG trigger for each frame, the hardware-based trigger delay (40–52 ms) and TE (8–10 ms) must be added to the frame time. For each cardiac-gated study, the RR interval reported in the figures and used in computations was the average RR interval during all the scans of the study.

Software

The MRIView program was developed on a Silicon Graphics (SGI, Mountain View, CA) Indigo Elan workstation using C, GL (SGI graphics language), X Window System, and Motif 1.2.3. It was designed to provide both a visual (qualitative) and numerical (quantitative) display of the flow data. Using the program, images were displayed in cross-sectional or 3D perspective view. For the perspective view, a 3D wireframe of the vessel boundary was generated by applying a 2D edge detection algorithm (explained below) in three orthogonal planes. In this view, there was full rotational, zoom, and clipping-plane capability. Particle paths, streamlines, and/or vector arrow maps of blood flow were overlaid on the wireframe or cross-sectional images. The path "clipping" option allowed the user to specify temporal and/or spatial segments of the paths to be displayed. Descriptive statistics, as shown in the tables, were derived from only the displayed portion of the particle paths.

Before particle path generation, background correction (i.e., resetting (to zero) of the phase value corresponding to zero velocity) was performed for each component of velocity, with a linear fit to x, y, and z of the phase values in pixels in nonflowing tissue around the vessel. Higher-order polynomial fits seemed to make no appreciable improvement in the flow patterns (although no quantitative analysis was performed).

Particle paths were generated by forward and/or backward numerical time integration starting from a user-defined sphere, cube, circular plate, or square at a particular time. Bilinear interpolation of the velocity data in

Table 1
Scan Parameters

Study description:						
Vessel(s):	Carotid	Basilar	Basilar aneurysm	Carotid	Aorta/renal	Coronary
Acquisition type:	3D	3D	3D	Sequential 2D	Sequential 2D	Sequential 2D
Cardiac gating:	Nongated	Nongated	Nongated	Gated	Gated	Gated
RF coil:	Anterior neck	CP head	CP head	Anterior neck	Quad spine	Quad body
Study number:	02019	01773	01884	02036	01968	08312
Scan parameters:						
Velocity encoding (cm/s):	120	40	60	110	120	40
Flip angle:	20°	20°	25°	30°	30°	25°
TR (ms):	36	25	24	36	33	33
TE (ms):	10.0	8.1	8.1	10.1	9.1	9.1
NEX:	1	1	1	2	2	2
x-FOV (mm):	120	180	180	120	240	200
y-FOV (mm):	120	180	180	120	240	200
z-FOV (mm):	29.7	41.3	41.3	18.0	43.0	3.6
Slice direction:	axial	axial	axial	axial	axial	coronal
Slice thickness (mm):	1.1	0.7	0.7	4.0	5.0	5.0
Slice interval (mm):	1.1	0.7	0.7	2.0	3.0	3.0
x-matrix size:	256	256	256	256	256	256
y-matrix size:	256	256	256	256	128	128
z-matrix size:	28	60	60	10	14	13
Frequency-encode direction:	A/P	A/P	A/P	R/L	R/L	R/L
Cardiac phases:				16	16	20
Average RR interval (ms):				730	811	1000
Trigger delay (ms):				52	40	40
Spatial resolution:						
x (mm):	0.469	0.703	0.703	0.469	0.938	0.781
y (mm):	0.469	0.703	0.703	0.469	1.875	1.563
z (mm):	1.1	0.7	0.7	2	3	3

CP head: circularly polarized birdcage head coil, x: frequency-encode direction, y: phase-encode direction, z: slice select or encode direction, A/P: anterior/posterior, R/L right/left, TE: automatically selected for shortest echo time at center of readout, slice interval: distance between adjacent slice centers, velocity analysis: three-direction encoding, phase-difference technique based on separate velocity encoded and nonencoded phase images. Scan options (all studies): autoshim on, flow compensation on, respiratory compensation on (renal, coronary only). Postprocessing options (all studies): phase correction off, gradient dewarping off, magnitude masking off.

both space and time, and a small fixed time step (0.003 s), was used for numerical integration. Smaller- and higher-order variable time step methods were also tested but were found to be unnecessary because the effective temporal resolution of the data was much longer (132–144 ms) than the implemented fixed step. The starting region was typically placed at a centralized location (both spatially and temporally) relative to the flow pattern being investigated. The user set the maximum length of time for forward and backward numerical integration, and integration was stopped automatically if the path moved out of the data set. Paths could also be started automatically at every frame in the cardiac cycle from the same spatial location. Display of these paths in a movie loop generally provided the most vivid visualization of the flow patterns.

The program contains several options for particular aspects of the velocity data. A common finding was wraparound of phase angle that occurred when the true velocity exceeded the preset velocity-encoded value (VENC) (14) corresponding to $\pm 180°$ phase accumulation. To visualize diastolic flow patterns, it was advantageous to pick a low VENC (between 40 and 60 cm/s), with the result that systolic velocities were severely wrapped. The program was designed to deal with this situation by automatically unwrapping the velocity measurements during particle path generation. Using this option required the path to be started in an unwrapped region. Also, when both high and low VENC images were acquired (e.g., 40 cm/s and 200 cm/s, with doubling of total examination time), the program was designed to use the high VENC image to determine the number of full wraps that occurred in the low VENC image (15). The program also provided a slice superposition option for visually adjusting the in-plane alignment of adjacent slices. In-plane shifting (by 1 or 2 pixels) was sometimes necessary to improve the alignment of tissue edges in adjacent slices, presumably a correction for subject motion. For detailed flow and velocity field statistical analysis of a small region of the data, the program provided a magnified cross-sectional "fragment" view.

Grayscale was used to encode the instantaneous speed, through-plane velocity, time of arrival relative to the starting point of the path, or time within the RR interval. When paths were overlaid on the cross-sectional images, the grayscale was used to reveal the location of the path relative to the displayed slice.

Manual particle path editing was performed to remove errant paths that exited the vessel through the wall, typically in focal areas of poor velocity data. The procedure consisted of displaying each particle path separately and choosing to either retain or delete the entire path. Groups of paths were defined by manual procedures similar to those used for editing and served to collect paths having particular temporal and/or spatial locations or particular features. The program was used to calculate descriptive statistics of the particle paths within each group, and the data were displayed graphically or in tabular form as a function of time, spatial location, or single path.

Starting points for the individual arrows of each arrow map were defined on an intraluminal Cartesian grid, with spacing and subpixel offset relative to the pixel centers set by the user. Spacing was typically set at 2–3 pixels along each in-slice direction; otherwise, the arrows were too densely packed. Forward and backward integrations were typically set at 0.008 s and 0.000 s, respectively, so at each slice the arrows were seen to propagate away from a flat surface. The step size of numerical integration was adjusted to fit a fixed number of steps (user-selected, typically six) to generate each arrow. Arrow locations covering the intraluminal volume were determined by amplitude thresholding, typically set to the same lower limit as used to construct the vessel wireframe.

The wireframes were generated based on an "amplitude threshold" (applied to the amplitude (i.e., signal magnitude) MR image as well as a "detail threshold" defined as the minimum number of discrete points in a polygon required for that polygon to be displayed. Polygons were generated by a 2D isoline algorithm, which determined both open and closed lines by local connectivity and linear interpolation of nearest neighbors around "seed" points defined initially at every voxel and which were then propagated (or not) based on the amplitude threshold value. Lower thresholds yielded larger and more coarsely outlined vessels, with more small polygons outside of the vessels. Particle paths tended to move slowly and wander outside the vessel if started at a peripheral location. To avoid excessive path editing, the thresholds were chosen such that the paths starting along the edge of the wireframe remained, for the most part (>85% retention), within the wireframe. Generally, this choice resulted in smooth wireframes just inside (≤ 1 pixel, all around) the "true" vessel wall, as identified by previously validated methods requiring gradient-recalled echo amplitude images (16) or requiring additional spin-echo images (17).

Horizontal circular wireframe lines representing the vessel boundary were placed at each slice location, and vertical wireframe lines were spaced on the boundary at each resolution element (pixel). In the nongated studies using 3D acquisition, the slices were equally spaced. The cardiac-gated studies involved more variable separation. In most arrow maps, the small arrows were difficult to see through both horizontal and vertical wireframe lines and so were shown with only horizontal wireframe lines.

Through-plane flow measurements (in cc/min) were computed from the arrow maps, at any particular slice location, as the average through-plane component of the velocity measured within the vessel and slice times the vessel cross-sectional area. The area estimate was defined by the number of whole pixels having amplitude above the same threshold used to determine the vessel wireframe. Flow measurements were also obtained directly from particle paths, at any particular slice location, using the average through-plane velocity times an estimate of the cross-sectional area covered by the paths. The formula $A = 2\pi^2 \langle\,|\,(x - \langle x \rangle)(y - \langle y \rangle)\,|\,\rangle$ was derived for the area A of the ellipse at each slice, where $\langle\,\rangle$ denotes numerical average over the paths within each slice. This formula was derived by equating the analytic integral of $|\,xy\,|$ over an ellipse centered at the origin, to its numerical approximation, the sum of $|\,(x - \langle x \rangle)(y - \langle y \rangle)\,|$ over the paths within the slice.

Quantitative descriptive analysis for each group of particle paths consisted of the number of individual paths and the average time duration, length, and speed of the paths. Also, two different standard deviation calculations were computed: (a) the average of the standard deviations of the speeds within each individual path, and (b) the standard deviation of the average speeds. The first standard deviation was large if the speed within each path varied considerably, and the second was large if there was a large variability in average speeds among the different paths. Specifically for the cardiac-gated flow measurements, the "interframe" standard deviation was defined as the square root of the average of the variances obtained at each of the frames in the cardiac cycle. In other words, it was the square root of the accumulated variance over the N frames, divided by N. The "interslice" standard deviation was defined as the square root of the variance of the average flow measured at each of the slice locations. Interframe and interslice standard deviations were roughly the same, but the latter was believed to be a less reliable measure of flow reproducibility, due to the limited number of samples (only one per slice location).

RESULTS

Representative flow patterns from the studies are shown in Figs. 1 through 5 and 7. Visualization parameters for all studies are listed in Table 2. Quantitative flow data for the particle paths are summarized in Table 3, and data for the descending aorta and renal artery arrow maps are summarized in Fig. 6 and Table 4.

Nongated Studies

Carotid Artery

Figure 1a shows streamlines traversing the carotid artery bifurcation in a 25-year-old female medical student in good health with no family or personal clinical history of arterial disease. The Superior/Inferior (S/I) length of vessel segment is 22.0 mm (slice thickness 1.1 mm; 20 slices in the figure). This figure shows distinct regions of rapid and slow flow in the carotid artery. It shows that within the anterior internal carotid artery (group II), speeds are 20–30 cm/s (average 25.51 cm/s) throughout the segment and similarly in the middle external carotid artery (group IV). In the posterior-inferior internal carotid artery (region of carotid bulb, group I), speeds are slower at 5–15 cm/s (average 8.58 cm/s) and streamlines are disorganized, but superiorly, these streamlines organize and attain velocities of 15–25 cm/s. Figure 1b shows the same streamlines with grayscale encoding for time of arrival. Paths with the highest speeds (along the anterior wall of the internal carotid artery and the external carotid artery) have only slight changes in gray value, indicating rapid traversal of the 2.2-mm segment (average duration 86.2 ms). Streamlines through the posterior carotid bulb were generated from the starting level (arrowhead) using as much as 150-ms forward and 150-ms backward time integration. These streamlines are black at the top of the figure, indicating slow speeds and the use of the full interval (0.24 s) to reach the superior border of the vessel

Table 2
Display Parameters

| | | | | | Figure | | | | | | | |
	1a, 1b	1c	1d	1e	1f	2a-2c	2d-2f	3	4	5a	5b	7
Vessel:	Carotid	Basilar	Basilar aneurysm	Basilar aneurysm	Basilar aneurysm	Carotid	Carotid	Aorta/renal	Aorta/renal	Aorta/renal	Aorta/renal	Coronary
Gating:	Nongated	Nongated	Nongated	Nongated	Nongated	Gated	Gated	Gated	Gated	Gated	Gated	Gated
Acquisition:	3D	3D	3D	3D	3D	Sequential 2D	Sequential 2D	Sequential 2D	Sequential 2D	Sequential 2D	Sequential 2D	Sequential 2D
Display:	Streamlines	Streamlines	Streamlines	Arrows	Arrows	Paths	Paths	Arrows	Paths	Arrows	Arrows	Paths
Study number:	02019	01773	01884	01884	01884	02036	02036	01968	01968	01968	01968	08312
Picture size, vertical (mm):	22.0	11.9	16.2	16.2	11.0	15.0 (a–e)	23.4 (f)	30.2	30.2	20.4	30.2	200
Picture size, horizontal (mm):	22.0	11.9	16.2	16.2	11.0	15.0 (a–e)	23.4 (f)	30.2	30.2	20.4	30.2	200
Spacing, vertical (mm):	1.1	0.7	0.7	0.7	0.350	2.0 (a–e)	0.469 (f)	3.0	3.0	0.938	0.938	0.781
Spacing, horizontal (mm):	0.469	0.703	0.703	0.527	0.352	0.469 (a–e)	0.469 (f)	1.406	0.938	0.938	0.938	0.781
Integration time, after (s):	0.150	0.150	variable	0.003	0.005	0.5	0.2	0.005	0.2	0.008	0.008	1.0
Integration time, before (s):	0.150	0.150	variable	0.0	0.0	0.5	0.2	0.0	0.2	0.0	0.0	1.0
Grayscale coding:	a: Speed b: TOA	Speed	Speed	Speed	Speed	Speed	d: Time e,f: Location	Speed	Speed	Speed	Speed	a: Speed b: Time
Time interval/frame (s):						0.0456	0.0456	0.0507	0.0507	0.0507	0.0507	0.05

TOA: time-of-arrival. Spacing: distance between adjacent wireframe lines for figures displaying streamlines or paths, between adjacent arrows for figures displaying arrows, and between pixel centers for figures displaying cross-sectional images.

Table 3
Flow Quantification of Particle Paths

	1a, 1b	1c	1d	2a–2c	2d–2f	4	7
				Figure			
Number of paths in group:							
Group I:	31	10	60	241	12	221	8
Group II:	18	10	19	104	11	178	8
Group III:	18	10	19	47			
Group IV:	21	10	9	32			
Group V:			9				
Average path duration(s):							
Group I:	0.235	0.043	0.175	0.067	0.302	0.245	1.396
Group II:	0.124	0.036	0.300	0.239	0.061	0.218	0.330
Group III:	0.216	0.051	0.055	0.490			
Group IV:	0.166	0.081	0.067	0.050			
Group V:			0.087				
Average path length (cm):							
Group I:	2.01	1.25	2.57	1.80	3.46	4.46	16.58
Group II:	3.15	1.41	2.77	2.21	1.94	4.47	2.74
Group III:	2.56	1.63	1.57	2.76			
Group IV:	3.27	1.79	1.83	1.80			
Group V:			1.55				
Average path speed (cm/s):							
Group I:	8.58	29.20	14.67	26.81	11.45	18.22	11.86
Group II:	25.51	39.33	9.25	9.25	31.60	20.47	8.31
Group III:	11.84	32.21	28.62	5.64			
Group IV:	19.72	22.12	27.19	35.89			
Group V:			17.86				
Standard deviation speeds within paths (cm/s):							
Group I:	6.79 (79%)	7.14 (24%)	13.22 (90%)	3.20 (12%)	8.06 (70%)	7.63 (42%)	14.74 (124%)
Group II:	3.67 (14%)	4.14 (11%)	4.71 (51%)	3.80 (41%)	12.37 (39%)	6.56 (32%)	3.31 (40%)
Group III:	6.72 (57%)	10.67 (33%)	14.64 (51%)	4.17 (74%)			
Group IV:	3.87 (20%)	5.26 (24%)	19.56 (72%)	6.64 (18%)			
Group V:			6.34 (35%)				
Standard deviation average path speeds (cm/s):							
Group I:	7.29 (85%)	0.47 (02%)	1.71 (12%)	4.26 (16%)	0.72 (06%)	8.36 (46%)	0.70 (06%)
Group II:	3.87 (15%)	1.61 (04%)	0.54 (06%)	1.97 (21%)	1.72 (05%)	6.46 (32%)	0.86 (10%)
Group III:	6.76 (57%)	1.95 (06%)	0.63 (02%)	1.25 (22%)			
Group IV:	4.54 (23%)	1.10 (05%)	2.62 (10%)	2.89 (08%)			
Group V:			0.34 (02%)				

Numbers in parentheses are standard deviations as percentage of average path speeds.

segment. These streamlines also failed to reach the bottom of the volume with backward time integration, indicating slow blood filling relative to the anterior region. Slow flow is also revealed (group III) along the posterior wall of the external carotid artery.

Basilar Artery Tip

Figure 1c shows normal basilar tip flow in a 23-year-old female medical student in good health with no family or personal clinical history of arterial disease. Four distinct streamline groups (I–IV) enter and course through the four terminal branches of the basilar tip. For each of these four groups, the starting spheres were placed at the ostia of the respective branch vessel, and the streamlines were propagated from these locations using no more than 150-ms forward and 150-ms backward time integration. The full S/I extent of this 60 slice 3D scan was 41.3 mm (the half-slice thickness beyond the slice 1 and slice 60 centers were not included because of the bilinear interpolation requirement). The basilar artery and branches extended over 28 slices, meaning that their S/I extent was 19.6 mm, but only the superior 17 slices (or 11.9 mm) of this volume are shown. By turning this perspective view

90° horizontally (not shown), it could be seen that the right superior cerebellar artery receives more of its flow from the posterior region of the basilar artery, whereas the corresponding left artery receives relatively more from the middle region. By overlaying these particle paths on the cross-sectional image at the junction of the four branches, or by turning this perspective view to look down on the basilar artery, it could be seen that these paths are in straight geometric alignment with the anatomical arrangement of the vessels. In other words, the paths do not twist around one another en route to their branch vessel. Unfortunately, flow just below the basilar artery tip could not be assessed because of poor (low signal-to-noise ratio (SNR)) velocity data; paths in that region did not remain within the vessel.

Basilar Artery Tip Aneurysm

In a basilar tip aneurysm in a 61-year-old female, the cross-sectional amplitude images from the nongated 3D phase-contrast angiographic study clearly showed the aneurysm body, the distal right posterior cerebellar artery (PCA), the proximal right PCA against the aneurysm body, and left PCA. In these images, the aneurysm body

Table 4
Renal Artery Flow Measurements

Vessel	Group	Average flow	Interframe standard deviation	Interslice standard deviation
Aorta above ostia	I	2126.1	39.7 (1.9%)	63.3 (3.0%)
Aorta between ostia	II	1608.7	52.3 (3.2%)	9.0 (0.6%)
Aorta below ostia	III	1075.6	27.6 (2.6%)	64.0 (5.9%)
Right renal	I–II	517.4	65.7 (12.7%)	63.9 (12.4%)
Left renal	II–III	533.1	59.1 (11.1%)	64.6 (12.1%)

All measurements in cc/min. Numbers in parentheses are standard deviations as percentage of total flow.

had high signal peripherally indicative of flow and low signal centrally indicative of slow flow or clot. Figure 1d shows the 3D perspective view of particle paths started in four distinct starting spheres at the base of the aneurysm (groups I and II) and near the ostia of the three adjoining vessels (groups III, IV, and V). Paths starting just right of center within the basilar artery (group I) are seen coursing directly into the aneurysm at a relatively high speed, impacting the superior wall, and then slowing down and flowing circumferentially toward the aneurysm center. The average speed of flow represented by these paths is 14.67 ± 1.71 cm/s, with relatively high standard deviation within the paths (13.22 cm/s, 90% of the average speed). The closed circumferential flow along the lateral wall of the aneurysm (group II) has an average speed of less than 9.25 cm/s. A portion of this flow returns from the aneurysm to supply, at higher speed, the lower left branch. This vessel also receives antegrade flow directly from the basilar artery (group V). Flow into the proximal right branches appears strong and not di-
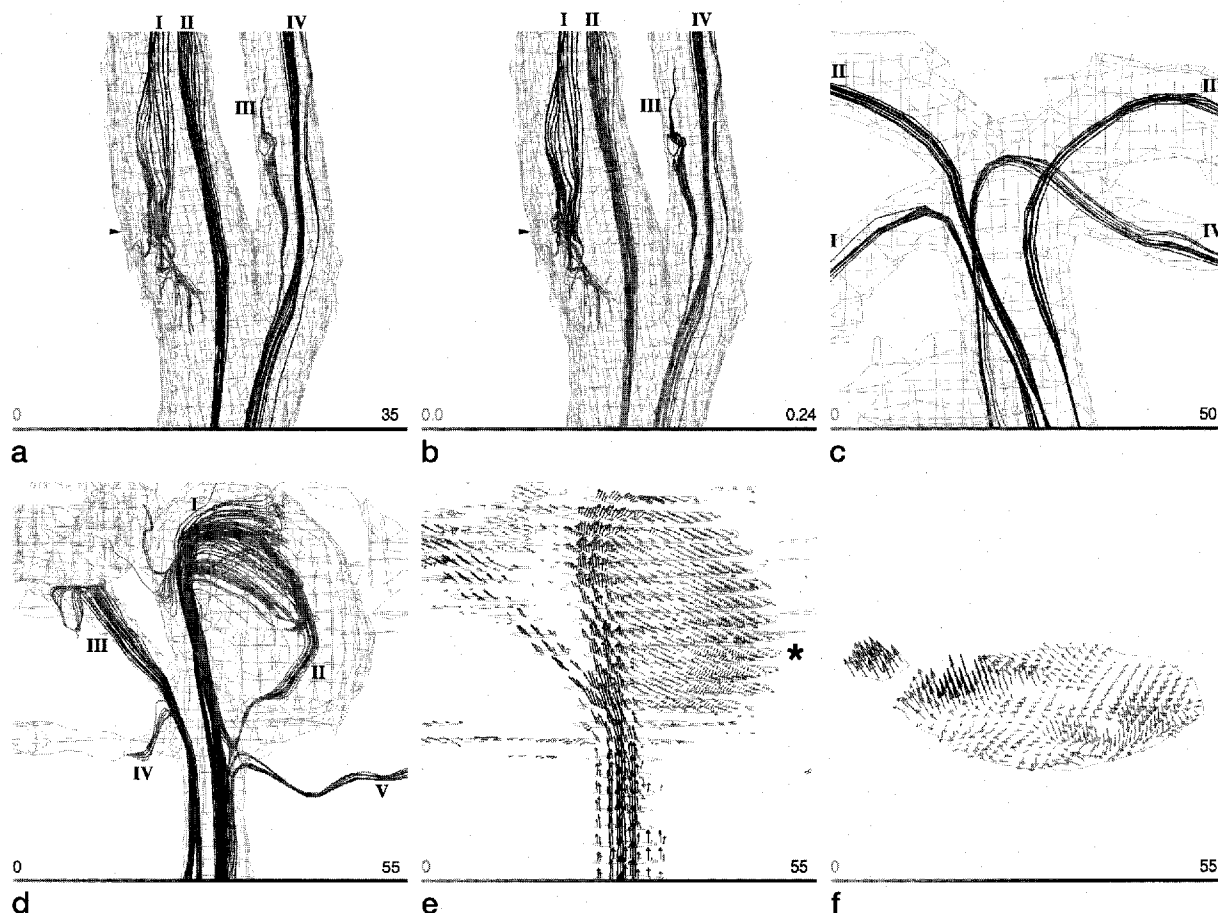

FIG. 1. Nongated flow studies (see Tables 1 through 3 for scan parameters, display parameters, and quantification). Wireframe derived using thresholding on the amplitude MR images (e.g., Fig. 2f). Roman numerals label streamline groups. (a) Normal right carotid artery bifurcation, lateral oblique view, with (0–35 cm/s) speed-encoded streamlines in posterior (I) and anterior (II) internal carotid arteries and external carotid artery (III, IV). Arrowhead marks starting location for group I streamlines. (b) Same vessel as in (a) with time of arrival (0.00–0.24 s) encoded streamlines. (c) Normal flow at apex of basilar artery, where it divides into right and left superior posterior cerebral arteries (II, III) and superior cerebellar arteries (I, IV), frontal view. The grayscale encodes speed from 0 to 50 cm/s. (d) Basilar artery apical aneurysm, frontal view, with streamlines showing antegrade flow into aneurysm (I), retrograde flow out of aneurysm (II), flow into three branch vessels (III, IV, V), and notable absence (obliteration) of proximal left posterior cerebral artery. The grayscale encodes speed from 0 to 55 cm/s. (e) Same study as in (d) with arrow map and same grayscale encoding. (f) Same study arrow map from single slice indicated by * in (e).

rectly hindered by the presence of the aneurysm, but distal flow is not tracked by these streamlines due to poor velocity data at the pixels where the paths terminate. The left posterior cerebellar artery wireframe is absent because the intraluminal amplitude of this vessel was below the chosen amplitude threshold. The left posterior cerebral artery did not appear to have direct contact with the aneurysm body. Not surprisingly, particle paths into the left posterior cerebral artery from the aneurysm or basilar artery were not found. However, on the cross-sectional amplitude images, continuity was found between this vessel and the posterior communicating artery.

The arrow map in Fig. 1e confirms the direction and speed of the streamlines revealed in Fig. 1d while allowing better assessment of flow in the intravascular regions immediately surrounding the streamlines. The full spatial extent of the low velocity (e.g., <9.25 cm/s) retrograde blood flow within the body of the aneurysm laterally is revealed, as is the stagnant central core. The left cerebellar vessel is not revealed because placement of an arrow at any given location requires that the underlying pixel amplitude be above the chosen threshold. Focal regions of poor velocity data are revealed in the right posterior cerebral and cerebellar vessels, at the location where the particle paths terminated in Fig. 1d.

Using the 3D perspective view, arrow maps at single slices were examined in greater detail at many orientations. The slice in Fig. 1f through the aneurysm body clearly shows the rapid forward flow region in the aneurysm medially, the retrograde flow region laterally, and the horizontal flow within the central region. In addition, the figure reveals the detailed structure of the circulating lateral (in-plane) flow in the aneurysm's central region. The flow has medial and lateral zones that are directed, respectively, toward the regions of forward flow entering deeper into the aneurysm and retrograde flow exiting the aneurysm.

Cardiac-Gated Studies

Carotid Artery

Figures 2a through 2c show particle paths generated from anterior, middle, and posterior internal carotid artery in a 25-year-old female medical student in good health without personal or family history of vascular disease. These figures show the significant difference in flow patterns found in the different regions of the internal carotid artery. Since all particle paths from all frames are displayed in each figure, these figures provide a compact display of the time-resolved flow patterns through the entire cardiac cycle but fail to convey the point in the cycle at which each pattern actually occurred. This information could, of course, be encoded in the grayscale instead of speed.

Figure 2a shows that blood flow in anterior internal carotid artery (group I) is shown to be steady and antegrade throughout the cardiac cycle. The average speeds of the individual particle paths are in a narrow range of 21.6–38.1 cm/s (average 26.8 ± 4.26 cm/s), and the standard deviation of speed within each path is small (16% of average). Figure 2b shows that the blood flow patterns in the middle internal carotid artery (group II) are more

complex. In particular, a helical flow pattern forms in the superior portion of vessel. The flow is much slower (average 9.25 ± 1.97 cm/s, range 6.65–14.19 cm/s), and the standard deviation within each path is much greater (41% of the average), indicating a more significant variation as a function of superior/inferior location and time point in the cardiac cycle. Figure 2c shows that blood flow in the posterior internal carotid artery (group III) has the most complex patterns. In the inferior portion (the carotid bulb), significant retrograde flow is revealed, but these particle paths organize into both helical and straight trajectories superiorly. Speeds are slowest and most variable in this group. The range of average speeds is 3.80–9.05 cm/s (average 5.63 ± 1.25 cm/s), and the average standard deviation within each path is greatest at 74% of the average. Figures 2d through 2h demonstrate different grayscale encodings of a flow pattern through the posterior internal carotid artery (labeled group I), and a strategy for display of paths on cross-sectional images. Paths through the central external carotid artery (labeled group II) are provided as a temporal reference for systole. In Fig. 2d, rapid flow is shown in the external carotid, and slower recirculating flow is shown through the middle and posterior internal carotid artery. The average speed for group I is 11.45 ± 0.72 cm/s, and the average speed for group II is 31.60 ± 1.72 cm/s. The standard deviation within paths for group I is 8.06 cm/s, or 70% of average, and the standard deviation within paths for group II is 12.37 cm/s, or 39% of average. These high standard deviations, particularly of the internal carotid paths, indicate that the speed of these paths changed significantly during the cardiac cycle. In Fig. 2e, particle paths are dark gray, light gray, and black, depending on whether they are within, above, or below the selected slice, respectively, as shown in Fig. 2f (marked by *). The paths are seen entering the slice anteriorly, coursing posteriorly and laterally within the selected slice around the periphery of the vessel, and then coursing inferiorly before merging with forward (antegrade) flow in the center of the vessel. Comparison with Fig. 2d shows that the paths move within the displayed slice during late systole and early diastole (dark gray sections) and flow antegrade out of the slice in diastole. The paths identify the signal loss in the center of the vessel as a region of antegrade flow.

Abdominal Aorta

Figures 3 through 6 show the abdominal aorta and renal artery flow in a 25-year-old female medical student in good health without personal or family history of renal artery disease. Cardiac-gated axial amplitude images (not shown) clearly showed the left and right renal arteries and the superior mesenteric artery branching from the descending aorta. Arrow maps were used to reveal local flow patterns in the descending aorta, whereas particle paths were used to investigate the pattern of flow into the renal arteries. Aortic flow was calculated in cc/min as a function of time, and the numbers compared qualitatively to the grayscale depiction of transverse velocity. Figure 3 shows arrow maps of descending aorta and renal arteries through the cardiac cycle. High flow in the de-
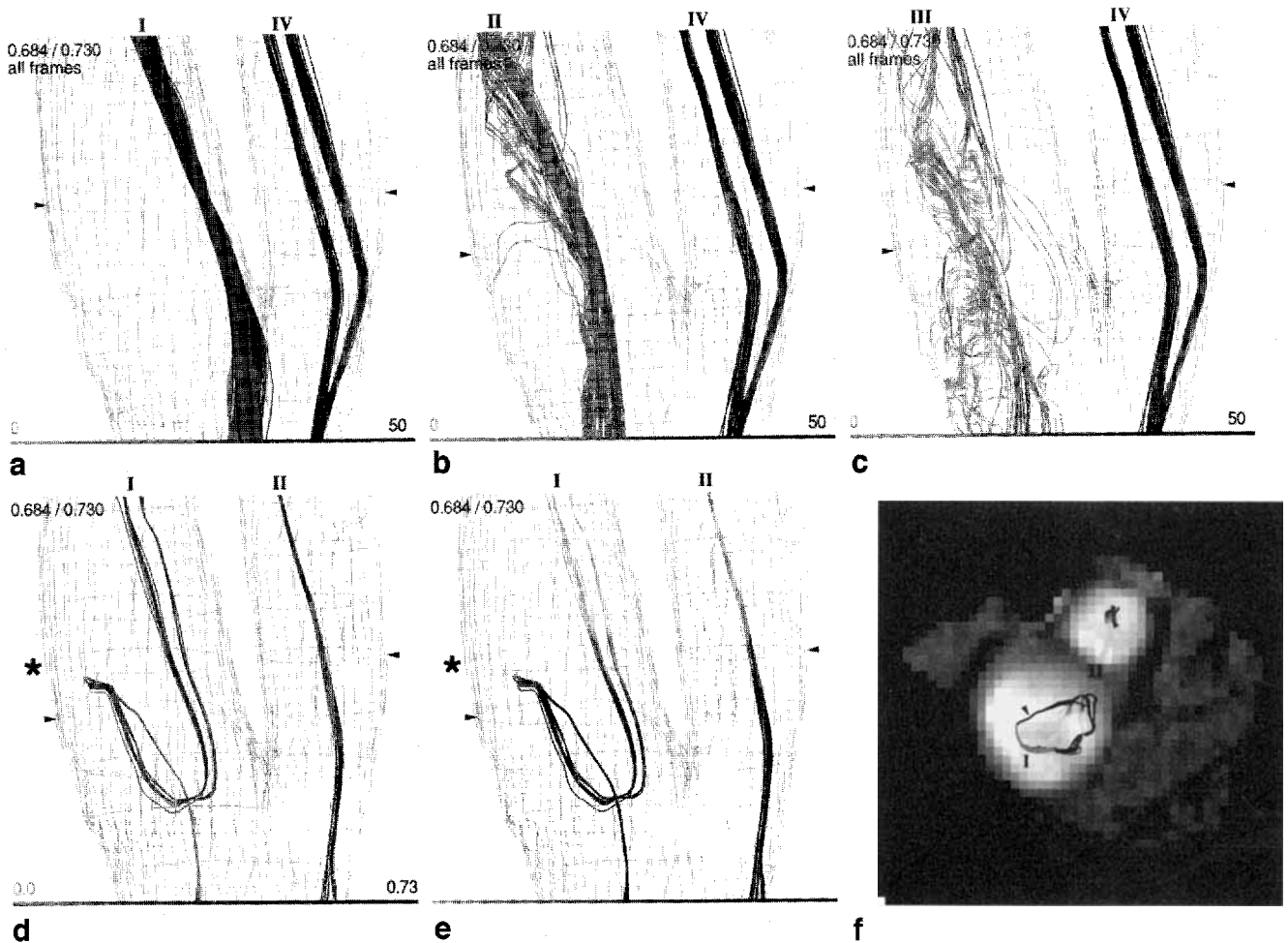
FIG. 2. Cardiac-gated carotid artery bifurcation flow study, normal subject, lateral oblique views (a–e). (See Tables 1 through 3 for scan parameters, display parameters, and quantification.) Wireframe derived using thresholding on amplitude MR images (f). Numbers in the top left corner indicate the frame time (in s) within the RR interval corresponding to the data used to create the wireframe, and the RR interval (0.730 s). Roman numerals label particle path groups. Paths in each group were started at the S/I location indicated by the adjacent arrowhead and integrated forward and backward in time. In (a–c), the grayscale encodes speed from 0 to 50 cm/s. The "all frames" annotation refers to the fact that paths in the internal carotid artery were started at every frame (16 in all) in the cardiac cycle. Particle paths in the external carotid artery (IV in a–c, II in d–f) were started only in frame 4 of 16 (in movie loops, these paths serve to mark systole). (a) Particle paths in anterior internal carotid artery (I); (b) particle paths in middle internal carotid artery (II); (c) particle paths in posterior internal carotid artery (III); (d) particle paths showing recirculating flow in middle and posterior internal carotid. The grayscale encodes time from 0.00 to 0.73 s within the RR interval. The starting point of the particle path (arrowhead) is in frame 4. (e) Same paths, now grayscale encoding of slice location: dark gray, light gray, and black, depending on whether the paths are within, above, or below the level marked by *. (f) Same paths, with same grayscale encoding as in (e), overlaid on the axial cross-sectional image corresponding to level marked by * in (e). (Darkened area surrounding vessel region is user-defined mask to restrict calculation of wireframes to only the (nondarkened) vessel region.)

scending aorta is seen in frames 3–7 with peak flow occurring in frame 5. Flow within the renal artery is slower than that in the descending aorta through peak systole but is better sustained through diastole (arrows are longer in the renal vessels compared to the central descending aorta). The infrarenal aorta has much less flow in mid- and late diastole (frames 9–16) compared to the suprarenal aorta. The vessel wireframe (derived using the same amplitude threshold at all frames) can be seen to expand in systole and contract in diastole. Changes in the wireframe dimensions depend not only on the physical change in wall location but also on changes in velocity profile along the wall that result in a change in the amount of phase dispersion signal loss. This signal loss is probably greater during systole, so the vessel diameter changes are probably underestimated.

To depict blood flowing into the renal arteries, particle paths were generated at every time point from starting spheres spanning the proximal portion of the ostia. Particle paths revealed features of the flow into the renal arteries that were suggested but not directly revealed by arrow maps. Figure 4 shows sustained flow throughout the cardiac cycle from the descending aorta into the left and right renal arteries. As seen on the arrow maps, the particle paths show that flow into both renal arteries is rapid throughout the cardiac cycle. However, the paths also reveal that flow into the renal arteries is strongly concentrated into a very narrow cross-sectional area in
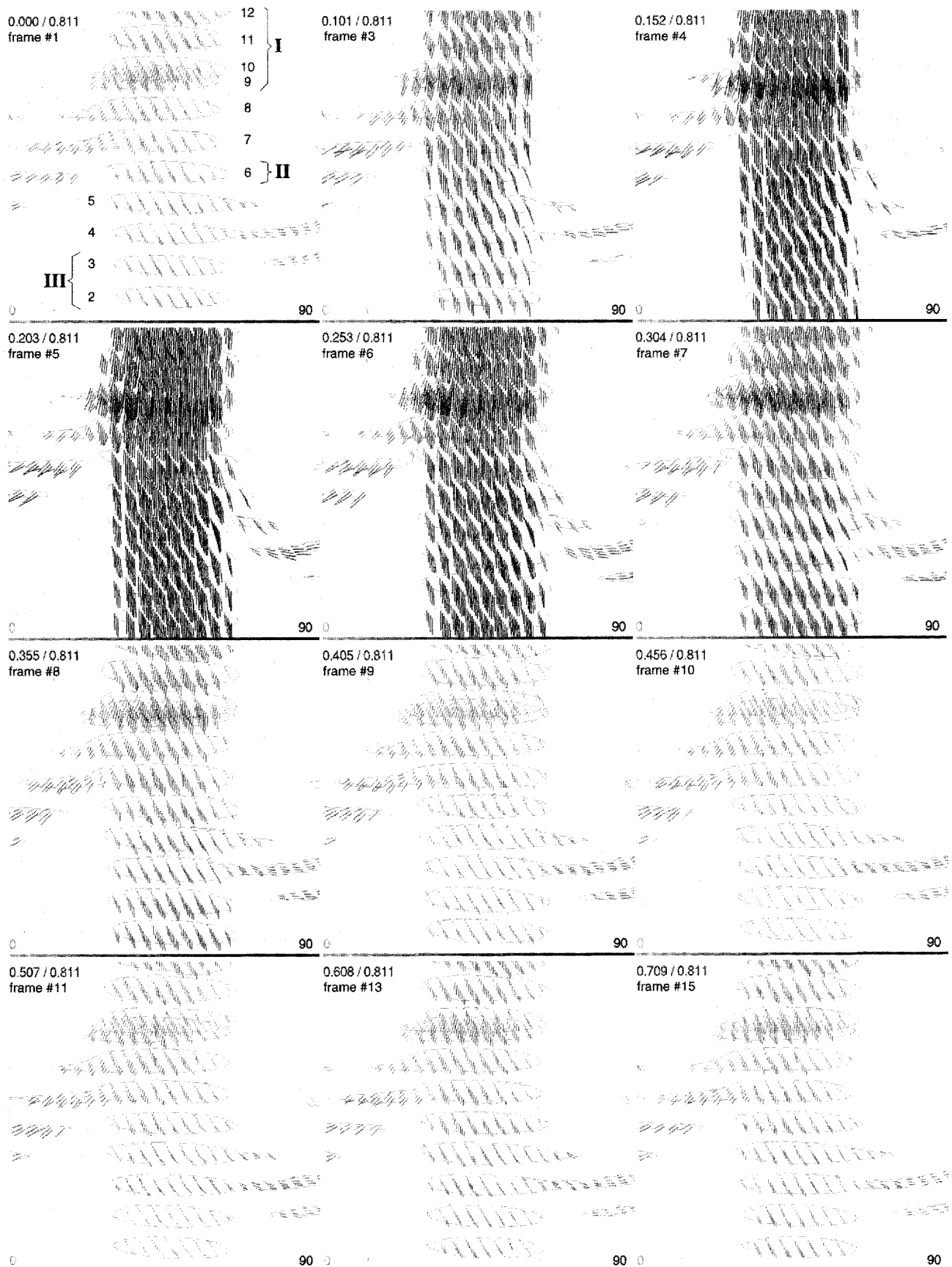
FIG. 3. Cardiac-gated descending aorta and renal artery flow study, normal subject, frontal view. (See Tables 1 and 2 for scan and display parameters and Table 4 and Fig. 6 for quantification.) Time sequence (frames 1, 3–11, 13, and 15 of 16) of arrow maps through the RR interval, with grayscale encoding of speed from 0 to 90 cm/s. The numbers in the top left corner give the frame time (in s) and the RR interval (0.811 s). Slice numbers and group assignments for those slice locations above (I), between (II), and below (III) the renal artery ostia are listed in frame 1.
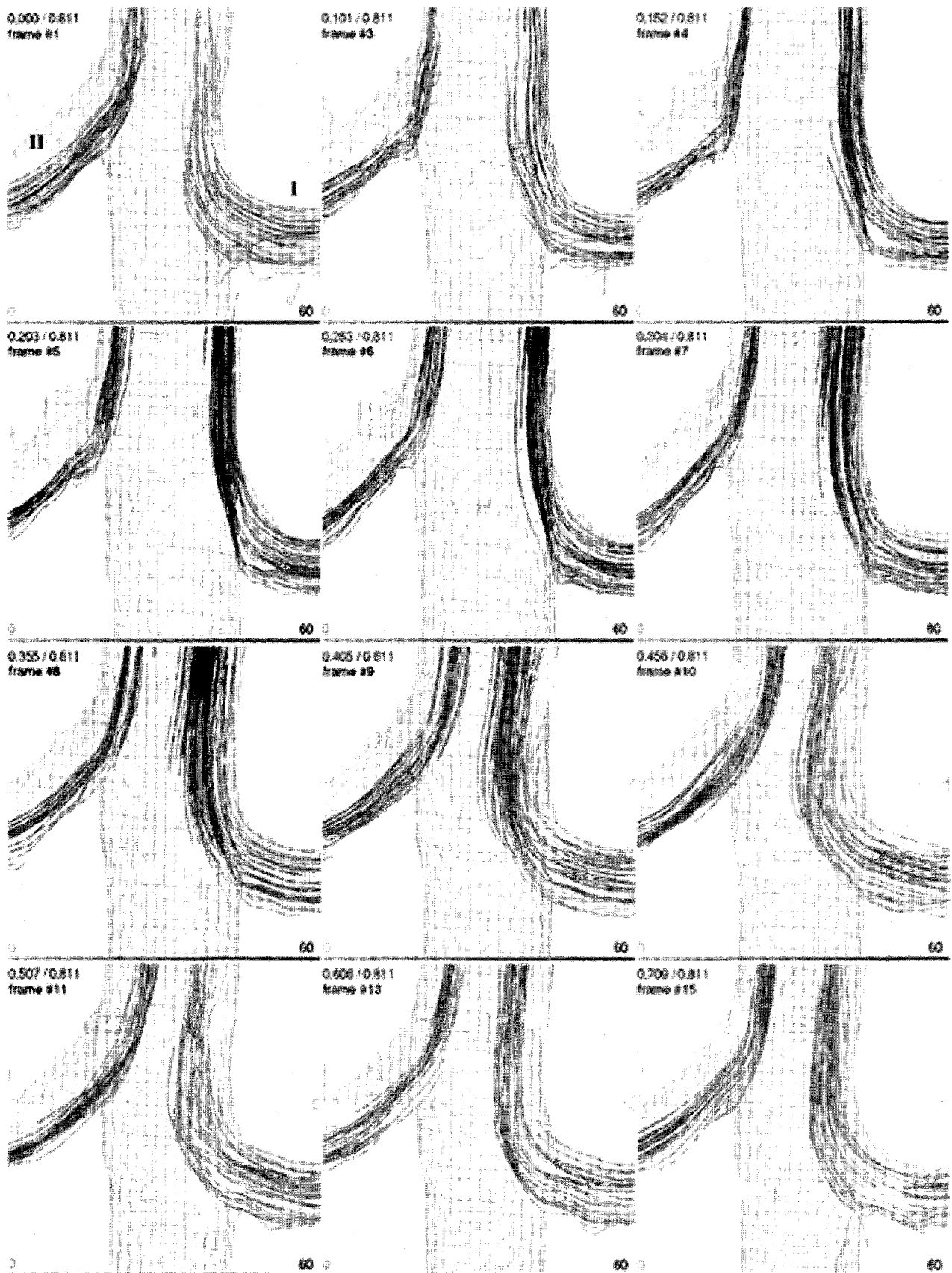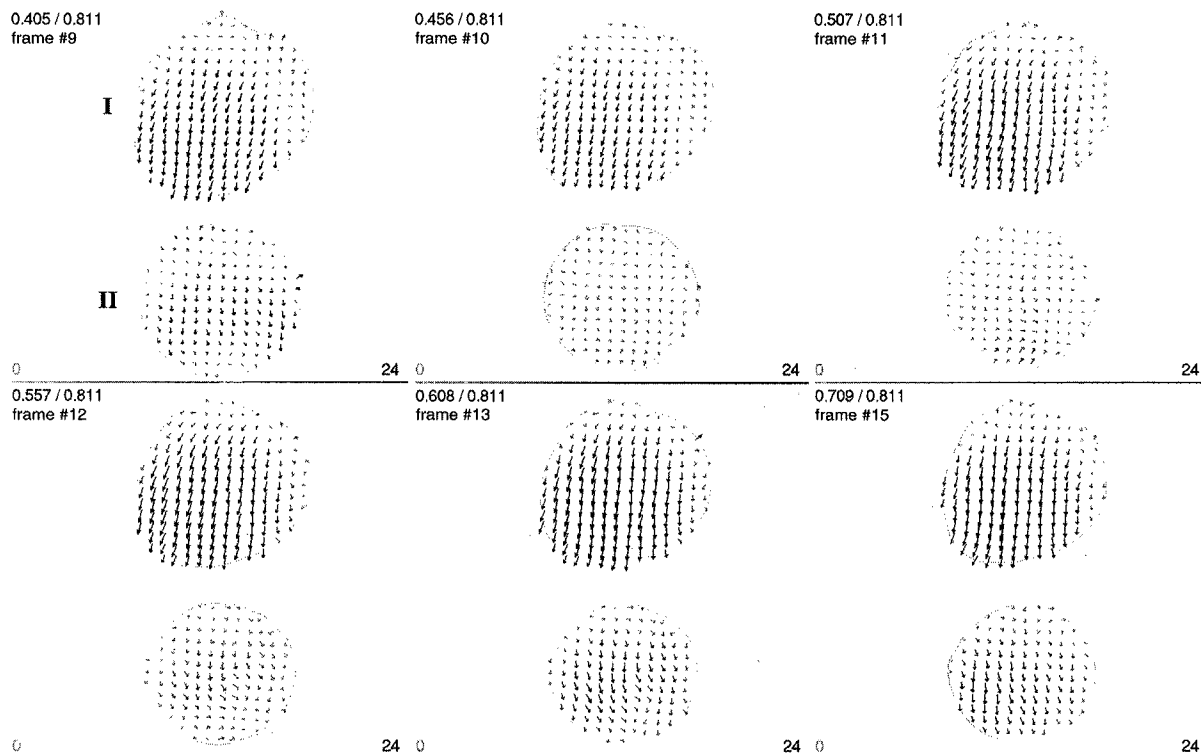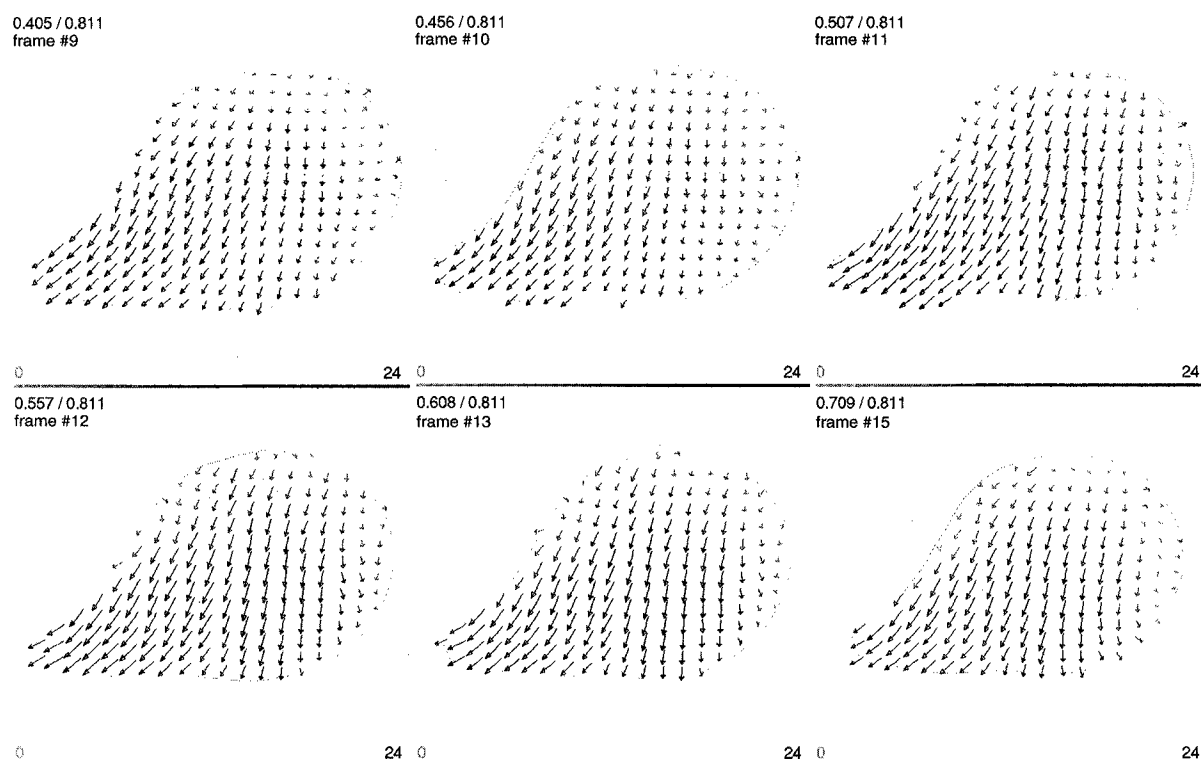
FIG. 4. Same study as in Fig. 3, with identical view, wireframes, frame timing, and RR interval. (See Tables 1 through 3 for scan parameters, display parameters, and quantification.) Time sequence (frames 1, 3–11, 13, and 15 of 16) of particle paths showing left (I) and right (II) renal artery flow through the cardiac cycle, with grayscale encoding of speed from 0 to 60 cm/s. Paths were started at both left and right renal ostia and integrated forward in time into the respective renal artery and backward in time into the descending aorta.

0.405 / 0.811
frame #9

0.456 / 0.811
frame #10

0.507 / 0.811
frame #11

I

II

0 24 0 24 0 24

0.557 / 0.811
frame #12

0.608 / 0.811
frame #13

0.709 / 0.811
frame #15

0 24 0 24 0 24

a

0.405 / 0.811
frame #9

0.456 / 0.811
frame #10

0.507 / 0.811
frame #11

0 24 0 24 0 24

0.557 / 0.811
frame #12

0.608 / 0.811
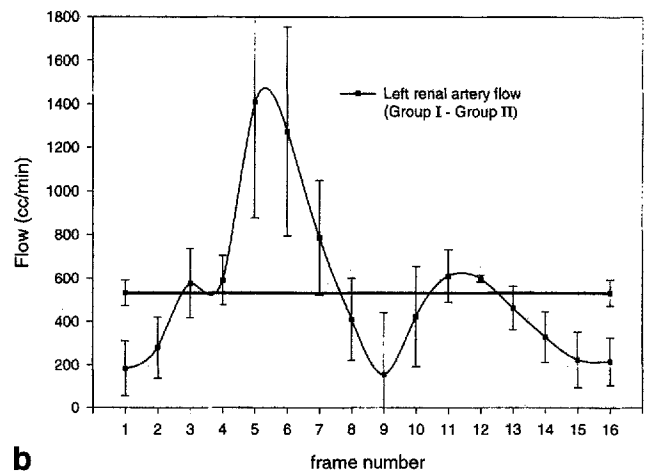frame #13

0.709 / 0.811
frame #15

0 24 0 24 0 24

b

FIG. 5. Same study as in Fig. 3, with identical wireframes, frame timing, and RR interval, inferior-frontal view. (See Tables 1 and 2 for scan and display parameters.) (a) Diastolic time sequence (frames 9–13, 15) of arrow maps at slice location above (I, slice 11 identified in frame 1 of Fig. 3) and below (II, slice 2 in Fig. 3) the renal artery ostia. The length of the arrows reveals the in-plane velocity, and the grayscale encoding gives the through-plane velocity from 0 to 24 cm/s. (b) Diastolic time sequence (frames 9–13, 15) of arrow maps at slice intersecting the right renal artery (slice 8 identified in frame 1 of Fig. 3). The length of the arrows reveals the in-plane velocity, and the grayscale encoding gives the through-plane velocity (cm/s) from 0 to 24 cm/s.
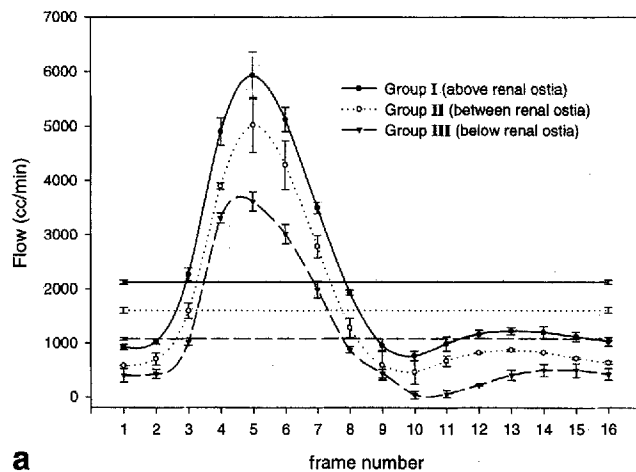
a

b
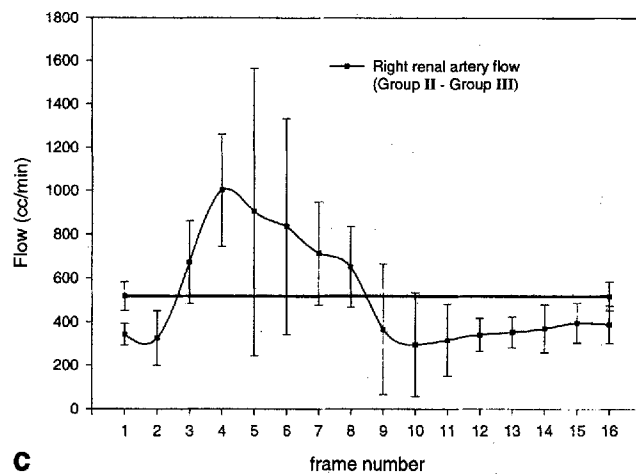
c

FIG. 6. Aortic flow quantification from arrow maps depicted in Fig. 3. Slice assignments for the groups are shown in frame 1 of Fig. 3. Mean and standard deviations of the flow measurements are plotted for each frame and each group (or group difference). The horizontal lines in each plot represent the net average flow; error bars represent the interframe standard deviation. (a) Flow (cc/min) versus time (frame number 1–16 in cardiac cycle) measured in slices lying above (slices 9–12, comprising group I), between (slice 6, comprising group II), and below (slices 2 and 3, comprising group III) the renal artery ostia. (b) Difference in flow between groups I and II to estimate right renal artery flow. (c) Difference in flow between groups II and III to estimate left renal artery flow.

the aorta during systole, and this cross-section increases significantly during diastole. This increase, which is more pronounced on the left side, begins in frame 7 and continues to the beginning of systole (frame 1). Retrograde flow in the descending aorta below the renal ostia into the left renal artery is seen in frames 15 and 1.

Flow is much more pulsatile in the descending aorta below the renal artery ostia. The difference in descending aorta flow above and below the renal artery ostia reflects a substantial flow into the renal arteries during diastole, supplied from the suprarenal aorta. Figure 5a shows diastolic frames for two descending aorta cross-sections, one above and the other below the renal artery ostia. In these images, the view of the vessel is from below and in front (inferior-frontal view), such that the bottom of the displayed image is posterior and the left is the subject's right side. The strongest flow in diastole is slightly right and posterior of center and is oriented above the renal artery. Flow along the left side of the aorta is relatively stagnant. This direct observation might have been expected based on Fig. 4, which showed the particle paths entering the left renal artery displaced away from the aortic wall. In the lower cross section (infrarenal aorta), speed and through-plane flow are greatly reduced, and there is a pattern of transverse (in-plane) swirling. Figure 5b shows diastolic frames of the cross section intersecting the right renal artery ostia are shown. The orientation is the same as in Fig. 5a. These frames show that sub-

stantial forward flow in the descending aorta is directed toward the right renal artery throughout diastole. Blood seems to be flowing into the right renal artery from at least half of the aorta's cross-sectional area. Similar features of diastolic flow were found in the left renal artery at slice 5 (not shown).

Figure 6a shows the through-plane flow versus time for arrow groups I, II, and III labeled in frame 1 of Fig. 3. It shows the consistency of the data from slice to slice and frame to frame and the difference in flow between slice locations above (group I), between (group II), and below (group III) the renal ostia. Figure 6b shows the difference between the flow in groups I and II, and Fig. 6c shows the difference between the flow in groups II and III. These differences estimate the right and left renal artery flow, respectively. For standard deviations of group II, which consists of only slice 6, slice 7 was used for additional data, with the spatial limits of the descending aorta defined to include left renal artery flow.

Results in Table 4 confirm that the flow measurements are reproducible, with interframe standard deviations of 1.86%, 3.25%, and 2.53% for descending aorta flow above, between, and below the renal ostia, respectively. Higher standard deviations for right and left renal artery flow (e.g., interframe deviations of 12.7% and 11.1%, respectively), are due to the much smaller average flow in each renal vessel and the summation of variance that results from taking the difference of aortic flows.

Flow measurements were also obtained from the particle paths shown in Fig. 4, but they represented only approximately 50% of the total flow in the vessels (see Discussion section). Average left renal artery flow, evaluated at slices 6–12, was 248.1 ml/min. Interframe and interslice standard deviations were 20.0 ml/min (8.1% of average flow) and 13.5 ml/min (5.5%), respectively. Average cross-sectional areas of these particle paths were 0.199 ± 0.025 cm^2 (interslice standard deviation), corresponding to radii of 0.251 ± 0.010 cm. Average right renal artery flow, evaluated at slices 9–12, was 196.2 ml/min. Interframe and interslice standard deviations were 17.6 ml/min (9.0% of average flow) and 22.0 ml/min (11.2%), respectively. Average cross-sectional areas of these particle paths were 0.155 ± 0.017 cm^2 (interslice standard deviation), corresponding to radii of 0.222 ± 0.011 cm.

Ascending Aorta and Coronary Artery

Flow patterns leading into the coronary arteries were revealed by starting particle paths within or at the base of the coronary artery ostia. Figures 7a and 7b show one example of flow from the left ventricle into the left anterior descending coronary artery in a 23-year-old male graduate student in good health without personal or family history of vascular disease. From the ventricle, paths first enter the root of the ascending aorta, followed by brief retrograde flow before stopping along the medial aspect of the aorta. Subsequently, the paths traverse the aorta horizontally in systole and enter the coronary artery in mid-diastole. Figure 7a reveals the highest speeds in the left ventricular outflow tract (≥ 90 cm/s) and the slowest speeds (average 8.31 ± 0.86 cm/s) within the left

main and anterior descending coronary artery. In Fig. 7b, the grayscale encodes time and shows that the paths travel from the ventricle in early/mid systole, rest in the lateral right aortic root through diastole, then traverse the aortic root in the subsequent systole to enter the left main coronary artery in mid-diastole.

DISCUSSION

This paper describes software and associated procedures for generating and processing large 3D velocity data sets of *in-vivo* blood flow in humans, to produce physically realistic, visually informative, and quantitatively precise time-averaged and time-resolved pictures of blood flow patterns. The project has lead to the observance of natural, unperturbed, human blood flow patterns never before described. In particular, the surging of early diastolic descending aorta flow into the renal arteries and the smooth and geometrically organized flow from the basilar artery into its four terminal branches have not been described previously with either extravascular or intravascular Doppler ultrasound or x-ray arteriography.

Arrow maps and particle paths have complementary roles in flow pattern visualization. These roles were best illustrated in the basilar artery aneurysm study and the descending aorta/renal artery study. Arrow maps showed how the blood is flowing everywhere in the volume, but arrow maps alone did not reveal (although time sequences of arrow maps did suggest) flow patterns defined over long time intervals. Particle paths showed these patterns but did not reveal accurately how much blood volume actually followed each pattern. The regularly spaced arrows of the arrow map, placed throughout the vessel lumen, best revealed the
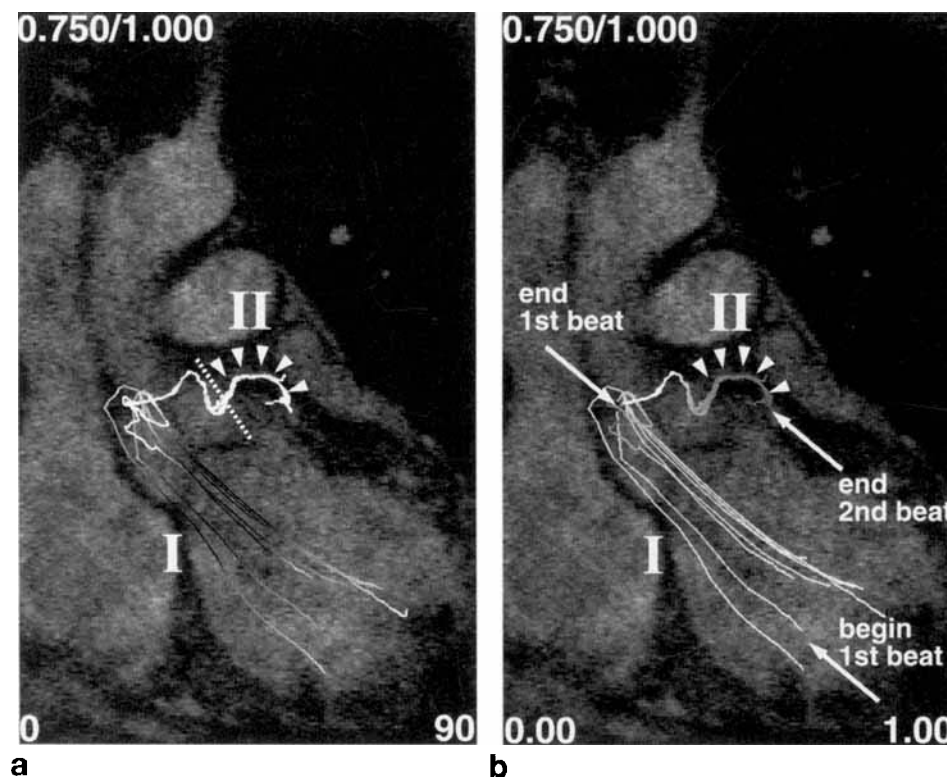

FIG. 7. Coronary artery flow study, normal subject. (See Tables 1 and 2 for scan and display parameters.) Particle paths are displayed on the diastolic coronal image (frame 15 of 20), which best showed the left coronary vasculature (arrowheads). The numbers in the top left corner give the frame time (in s) of the displayed image and the RR interval (1.00 s). Particle paths reveal left main and left anterior descending coronary artery flow arising from the left ventricle. Paths are divided by the dotted line into ventricle-aorta group (I) and coronary artery group (II). This line also marks the starting location of the paths. (a) The grayscale encodes speed from 0 to 90 cm/s. (b) The grayscale encodes time from 0.00 to 1.00 s across the RR interval. Arrows identify positions corresponding to the beginning and end of the heartbeats in this two-beat pattern.

a   b

total volume of blood after each pattern. Particle paths, because they were generated over long time intervals, accumulated positional error and became unreliable upon passing through low-velocity zones. Therefore, they were not as good as arrow maps for assessing flow near the walls and in remote corners of the vasculature. They were more likely to produce inaccurate estimates of the average flow in vessels, due to the editing out of those paths in these regions that erroneously exited through the vessel wall.

Although it was not the intent of this project to compile population data on flow patterns, it was reassuring to find patterns consistent with previous studies. In the basilar artery study, streamlines demonstrated geometrically aligned flow into each of the terminal branches. The distinctive pattern of left superior cerebellar artery blood first rising toward the tip of the basilar artery and then flowing retrograde into the vessel had been reported previously in normal subjects (18). Characteristic features of basilar artery aneurysm flow patterns revealed in our study included (a) high-velocity flow from the basilar artery to the apex of the aneurysm; (b) subsequent slow swirling flow toward the center of the aneurysm, with blood stasis in the center; and (c) recirculation around the periphery of the aneurysm back to the terminal branches. These features were noted previously in a study that used a precisely cast model of an excised basilar artery aneurysm and investigated flow patterns within the models using video recording of colored dye streams, MR time of flight, and MR phase contrast angiography (19).

Particle paths in the posterior internal carotid arteries generated from the cardiac-gated data clearly showed time-resolved flow patterns commonly observed with Doppler ultrasound, such as late systolic and diastolic recirculating flow, stasis, and chaotic flow in the inferior bulb opposite the flow divider and helical flow in the posterior-superior portion of the internal carotid artery (20–22). The streamlines in Fig. 1 derived from *nongated* velocity data also suggested these patterns. The flow patterns observed in the inferior bulb are associated with low and oscillatory wall shear stress, which are important in the pathogenesis of atherosclerotic plaque, and plaque in the carotid most often forms at this location (23–25). The anterior internal carotid arteries, which are normally spared atherosclerotic disease, showed relatively constant and rapid flow that is associated with high constant shear stress, which is considered to be protective against plaque.

In the descending aorta, particle paths showed significantly less antegrade flow, and more lateral circulating and retrograde flow, below versus above the renal artery ostia. Previous MR studies using cardiac-gated 2D velocity encoding have also reported retrograde flow and oscillating shear stress (inferred from velocity vectors at the wall) in the infrarenal aorta in normal subjects, with relatively smooth antegrade flow immediately above the ostia (26, 27). These observations are consistent with the well-known fact that infrarenal aorta flow patterns are more complex than those in the suprarenal aorta and that they are probably responsible for the increased susceptibility of the infrarenal aorta to atherosclerosis (28–30).

The coronary arteries are unique in that much of their flow appears to come from retrograde aortic flow in diastole (31, 32). Using intraarterial Doppler ultrasound (33) and phase-contrast MRI (34, 35), the highest coronary artery flow velocities were typically seen in early to mid-diastole. Our coronary artery studies also revealed the highest flow in early and mid-diastole. The unusual pattern over two heartbeats displayed in Fig. 7 is, in fact, similar to those shown by Ohlsson in dogs using fluoroscopy (31). To the author's knowledge, there are no other references on the tracking of blood flow from the ventricle into the coronary arteries.

The renal artery flow measurements obtained from the arrow maps summarized in Table 4 were within expectations based on previous studies using cardiac-gated velocity-encoded phase imaging (36–39). In these previous studies, renal artery flow was measured based on the difference between aortic flow measurements above and below the renal artery ostia and by direct measurement within the renal arteries. In a total of 28 subjects, the average of the average renal artery flow measured by aortic flow was 1140 ml/min (range 991–1320 ml/min) and the average of the standard deviations in each study population was 308 ml/min (range 245–360 ml/min). In a total of 36 subjects, the average of the average direct renal artery flow measurement was 1211 ml/min (range 1125–1428 ml/min), and the average of the standard deviations in each study population was 322 ml/min (range 159–540 ml/min). In two of the studies (37, 38), *p*-aminohippurate clearance measurements of renal artery flow were also obtained, and were 4% and 17% (both lower) than the direct renal artery flow measurements.

Flow computed from the renal artery particle paths was only 40–50% of the value obtained from the aortic arrow maps. The reason for this could be traced to the small cross-sectional area covered by the particle paths relative to that of the vessel. Due to subtleties of the signal amplitude changes in the presence of slow flow, renal artery cross-sectional areas were difficult to assess, even on sagittal-oblique images oriented perpendicular to the vessel. Previous studies (36–39) reported a wide range of average renal artery diameters in their study populations: 0.645–1.002 cm^2 for the left and 0.643–1.046 cm^2 for the right renal artery. The standard deviations within each study were much less (typically 0.04 cm^2) than the variation across studies, indicative of a general lack of consensus on methodology and the vessel's small size. In our axial amplitude images (showing the renal arteries cut along their long axis), the left and right renal artery diameters at the ostia were approximately 8 pixels (0.750 cm) and 7 pixels (0.656 cm), respectively. However, the diameters of the particle path cross sections were only approximately 5 pixels and 3.5 pixels. Thus, the paths actually examined only the central 62.5% (5/8) and 50.0% (3.5/7) of the entire vessel cross section. Therefore, it was not unexpected that the flow totaled only a fraction of the average flow in the artery. Based on a laminar flow distribution, the central 62.5% and 50.0% of a vessel diameter has only 62.9% and 43.8% of the flow, respectively. These percentages are lower (39.1% and 25%) when based on a plug flow distribution. The particle path flow estimates were

46.5% and 37.5% of that obtained using the aorta arrow maps—the true flows are probably between those predicted by the laminar and plug flow distributions.

To estimate through-plane flow, we used the established phase-difference technique for measurement of velocity from the phase images and simple summing of the areas of pixels having amplitude values above the preset threshold. A previous review of the literature reported flow accuracy and precision (as measured by standard deviation of the mean flow) of these methods in large vessels to be 5–10% (40), e.g., 7.6% reported in ref. 16 and 5.9% reported in ref. 41. Alternative techniques for flow measurement based on complex differencing (42), subtraction strategies that theoretically improved measurement accuracy but compromised SNR (i.e., precision) (43), or strategies requiring three velocity encodings (and 50% more scan time) (44) were also considered. These alternatives claimed to reduce flow errors by virtue of reducing partial voluming of blood with stationary tissue along the vessel edge, but were not used due to the fact that they would have had only a small effect in the larger vessels, and due to the mentioned tradeoffs.

Some distortion of our velocity data may stem from spatial and velocity displacements in the phase-contrast measurements, due to small (3–8 ms) temporal offsets of spatial and velocity encoding within each TR interval. The effects of these offsets have been analyzed, in phantoms, in a recent study (45). It is important to emphasize that the effects were generally small and unlikely to be the primary distortions in our flow patterns. The most serious distortions of our flow patterns are most likely due to (a) the acquisition of baseline, v_x, v_y, and v_z data sequentially over multiple TR periods (e.g., separated by as much as 99 ms), (b) the interpolation of each velocity component across four TR periods (e.g., 132 ms), and (c) the acquisition of data over multiple heartbeats under the assumption that the flow pattern is periodic. The recent paper avoided these distortions by considering only steady flow.

Although the data acquisition and visualization capabilities of MRI are substantial, it is important to identify fundamental limitations and areas where improvements are needed. MRI will never provide the millisecond temporal resolution, real-time capabilities of Doppler ultrasound. Generally, MRI will continue to have temporal delays between velocity and spatial encoding and rely on data acquisition over multiple heartbeats. Use of single-shot velocity-encoded echo-planar or spiral imaging, with 100- to 150-ms temporal resolution, will allow detection of nonperiodic flow patterns, better visualization of periodic flow patterns, and better analysis of distortions resulting from the use of multiple heartbeats, but spatial resolution (e.g., maximum matrix sizes of 128 × 128) will be somewhat limited. With respect to improvements, an efficient, time-resolved 3D velocity-encoded pulse sequence is needed to maximize acquisition efficiency. The total acquisition time for collection of the time-resolved 3D data set was typically 60 min (about 256 s per slice location, based on 1 beat/s, and 15 slice locations). This can easily be reduced to less than 15 min using short TR 3D acquisitions, reduced FOV, and reduced number of phase-encode steps in two of three

directions. Temporal resolution of the current sequences is poor (e.g., 132 ms) but can be reduced by a factor of two with halving of TR. Improvements and innovations for data processing software include programs to (a) enforce momentum conservation on the experimental velocity data, and (b) compute particle paths probabilistically rather than deterministically.

The connection of atherosclerosis with hemodynamics (particularly flow conditions leading to low and/or oscillatory shear stress at the vessel wall (e.g., ref. 46)) and such shear stress leading to atherosclerosis (e.g., refs. 25, 47, and 48) has had little impact in the clinical setting. Because atherosclerosis is a slow but chronically developing process, the connection between flow patterns and the formation and evolution of atherosclerotic lesions will be difficult to establish clinically. Nevertheless, the Pathobiological Determinants of Atherosclerosis in Youth (PDAY) study confirmed that atherosclerosis development occurs at an early age (49, 50) and it is worthwhile to have ready a noninvasive detection method to track serious cases starting at an early age. MR visualization and quantification of flow patterns may also have value for evaluation and follow-up of vascular interventional procedures, given the present use of Doppler ultrasound in assessing vascular interventional complications (51–56), and the importance of flow patterns in mediating the anastomotic endothelial response (57).

It has been argued that, since abnormal forces that initiate and promote atherosclerosis act at the vessel wall, measurements of these forces must be made at the vessel wall (e.g., within 30–100 μm). Unfortunately, reliable in-vivo MRI measurement of shear stress and strain at the wall in humans is probably not possible at that spatial resolution. Previous attempts to obtain subpixel spatial resolution have required special data processing and signal and flow modeling (26, 58–61). It is likely that global flow patterns can be measured reliably using standard MRI spatial and temporal resolutions (e.g., 0.5 mm, 30 ms). In fact, the MRIView software development has been motivated by the belief that flow patterns measured at standard resolutions will be sufficient to indirectly infer (using fluid dynamical principles) accurate estimates of shear stress and other parameters at the vessel wall. Algorithms that force the experimental velocity data to be consistent with laws of mass (divergence) and momentum (Navier-Stokes) conservation could produce these estimates. Several groups have used computational fluid dynamics to compute the flow of blood magnetization within vessel models, and have compared time-of-flight amplitude and velocity encoded phase images obtained from the simulation, with corresponding amplitude and phase images obtained from in-vivo MRI (e.g., 62–66). However, direct numerical processing of time-resolved 3D MRI velocity fields, such that the fields become consistent with fluid mechanics laws, has been reported only recently (67). It appears that computational fluid dynamics, with constraints determined by MRI velocity data, is likely to provide the most accurate representation of blood flow, and this the focus of much current work.

REFERENCES

1. S. Napel, D. H. Lee, R. Frayne, B. K. Rutt, Visualizing three-dimensional flow with simulated streamlines and three-dimensional phase-contrast MR imaging. *J. Magn. Reson. Imaging* **2**, 143–153 (1992).

2. M. H. Buonocore, Algorithms for improving calculated streamlines in 3-D phase contrast angiography. *Magn. Reson. Med.* **31**, 22–31 (1994).

3. R. H. Mohaiddin, G. Z. Yang, P. J. Kilner, D. B. Longmore, Visualization of flow by vector analysis of multidirectional cine MR velocity mapping: technique and application. *J. Magn. Reson. Imaging* **3(P)**, 26 (1993).

4. P. J. Kilner, G. Z. Yang, R. H. Mohiaddin, D. N. Firmin, D. B. Longmore, Helical and retrograde secondary flow patterns in the aortic arch studied by three-directional magnetic resonance velocity mapping. *Circulation* **88(5 Pt 1)**, 2235–2247 (1993).

5. H. G. Bogren, R. H. Mohiaddin, G. Z. Yang, R. J. Kilner, D. N. Firmin, Magnetic resonance velocity vector mapping of blood flow in thoracic aortic aneurysms and grafts. *J. Thorac. Cardiovasc. Surg.* **118**, 704–714 (1995).

6. R. H. Mohiaddin, Flow patterns in the dilated ischemic left ventricle studied by MR imaging with velocity vector mapping. *J. Magn. Reson. Imaging* **5**, 493–498 (1995).

7. M. H. Buonocore, Visualizing flow into the coronary arteries using streamlines, *in* "Proc., Scientific Conference on the Application of Magnetic Resonance to the Cardiovascular System, American Heart Association, Atlanta, 1993," p. 20.

8. M. H. Buonocore, Visualizing flow patterns in the ascending aorta using streamlines. *J. Magn. Reson. Imaging* **4(P)**, 94 (1994).

9. M. H. Buonocore, Using streamlines to interpret data from 3D phase contrast magnetic resonance angiography. *Radiology* **193(P)**, 387 (1994).

10. M. H. Buonocore, I. Aleinov, Streamline visualization of flow patterns implicated in the pathogenesis of atherosclerosis, *in* "Proc., SMR, 3rd Annual Meeting, Nice, 1995," p. 88.

11. M. H. Buonocore, Processing, analysis and display of time-resolved 3D velocity encoded MRI data, *in* "Proc., ISMRM, 4th Annual Meeting, New York, 1996," p. 1648.

12. M. H. Buonocore, Strategies for display of velocity fields of blood flow obtained using MRI. *Radiology* **201(P)**, 193 (1996).

13. N. J. Pelc, M. A. Bernstein, A. Shimakawa, G. H. Glover, Encoding strategies for three-direction phase-contrast MR imaging of flow. *J. Magn. Reson. Imaging* **1**, 405–413 (1991).

14. N. J. Pelc, Flow quantification and analysis methods, *in* "Magnetic Resonance Imaging Clinics of North America: MR Angiography of the Central Nervous System" (A. W. Litt, Ed.), pp. 413–424, WB Saunders, Philadelphia, 1995.

15. A. T. Lee, G. B. Pike, N. J. Pelc, Three-point phase-contrast velocity measurements with increased velocity-to-noise ratio. *Magn. Reson. Med.* **33**, 122–126 (1995).

16. M. H. Buonocore, H. G. Bogren, Factors influencing the accuracy and precision of velocity encoded phase imaging. *Magn. Reson. Med.* **26**, 141–154 (1992).

17. M. H. Buonocore, H. G. Bogren, Optimized pulse sequences for magnetic resonance measurement of aortic cross sectional areas. *Magn. Reson. Imaging* **9**, 435–447 (1991).

18. T. Karino, H. Goldsmith, M. Motomiya, Flow patterns in vessels. *Ann. N. Y. Acad. Sci.* **516**, 422–441 (1987).

19. B. W. Chong, C. W. Kerber, R. B. Buxton, L. R. Frank, J. R. Hesselink, Blood flow dynamics in the vertebrobasilar system: correlation of a transparent elastic model and MR angiography. *AJR* **15**, 733–745 (1994).

20. D. N. Ku, D. P. Giddens, D. J. Phillips, D. E. Strandness Jr., Hemodynamics of the normal carotid bifurcation: in vitro and in-vivo studies. *Ultrasound Med. Biol.* **11**, 13–26 (1985).

21. D. J. Phillips, F. M. Greene, Y. Langlois, G. O. Roederer, D. E. Strandness Jr., Flow velocity patterns in the carotid bifurcation of young, presumed normal subjects. *Ultrasound Med. Biol.* **9**, 39–49 (1983).

22. W. D. Middleton, W. D. Foley, T. L. Lawson, Flow reversal in the normal carotid bifurcation: color Doppler flow imaging analysis. *Radiology* **167**, 207–210 (1988).

23. C. K. Zarins, D. P. Giddens, B. K. Bharadvaj, V. S. Sottiurai, R. F. Mabon, Carotid bifurcation atherosclerosis, quantitative correlation of plaque localization with flow velocity profiles and wall shear stress. *Circ. Res.* **53**, 502–514 (1983).

24. P. A. Beere, S. Glagov, C. K. Zarins, Experimental atherosclerosis at the carotid bifurcation of the cynomologus monkey: localization,

25. compensatory enlargement, and the sparing effect of lowered heart rate. *Arterioscler. Thromb.* **12**, 1245–1253 (1992).

25. D. P. Giddens, C. K. Zarins, S. Glagov, The role of fluid mechanics in the localization and detection of atherosclerosis. *J. Biomech. Eng. (Trans. ASME)* **115(4B)**, 588–594 (1993).

26. J. N. Oshinski, D. N. Ku, S. Mukundan, F. Loth, R. I. Pettigrew, Determination of wall shear stress in the aorta with the use of MR phase velocity mapping. *J. Magn. Reson. Imaging* **5**, 640–647 (1995).

27. G. H. Mostbeck, M. C. Dulce, G. R. Caputo, E. Proctor, C. B. Higgins, Flow pattern analysis in the abdominal aorta with velocity encoded cine MR imaging. *J. Magn. Reson. Imaging* **3**, 617–623 (1993).

28. J. E. Moore, D. N. Ku, C. K. Zarins, S. Glagov, Pulsatile flow visualization in the abdominal aorta under differing physiologic conditions: implications for increased susceptibility to atherosclerosis. *J. Biomech. Eng. (Trans. ASME)* **114**, 391–397 (1992).

29. P. K. Wong, K. W. Johnston, C. R. Ethier, R. S. Cobbold, Computer simulation of blood flow patterns in arteries of various geometries. *J. Vasc. Surg.* **14**, 658–667 (1991).

30. K. B. Chandran, Flow dynamics in the human aorta. *J. Biomech. Eng. (Trans. ASME)* **115**, 611–616 (1993).

31. N. M. Ohlsson, Left heart and aortic blood flow in the dog. *Acta Radiol. Suppl.* **213**, 1–75 (1962).

32. H. G. Bogren, R. H. Mohiaddin, R. H. Klipstein, D. N. Firmin, R. S. Underwood, S. R. Rees, D. B. Longmore, The function of the aorta in ischemic heart disease: a magnetic resonance and angiographic study of aortic compliance and blood flow patterns. *Am. Heart J.* **118**, 234–247 (1989).

33. R. F. Wilson, D. E. Laughlin, P. H. Ackell, W. M. Chilian, M. D. Holida, C. J. Hartley, M. L. Armstrong, M. L. Marcus, C. W. White, Transluminal, subselective measurement of coronary artery blood flow velocity and vasodilator reserve in man. *Circulation* **72**, 82–92 (1985).

34. M. B. Hofman, A. C. van Rossum, M. Sprenger, N. Westerhof, Assessment of flow in the right human coronary artery by magnetic resonance phase contrast velocity measurement: effects of cardiac and respiratory motion. *Magn. Reson. Med.* **35**, 521–531 (1996).

35. J. N. Oshinski, R. Y. Hahn, K. Seibert, R. I. Pettigrew, Navigator echo gated coronary flow measurements, *in* "Proc., ISMRM, 5th Annual Meeting, Vancouver, 1997," p. 108.

36. B. Lundin, T. G. Cooper, R. A. Meyer, E. J. Potchen, Measurement of total and unilateral renal blood flow by oblique-angle velocity encoded 2D-cine magnetic resonance angiography. *Magn. Reson. Imaging* **11**, 51–59 (1993).

37. R. L. Wolf, B. F. King, V. E. Torres, D. M. Wilson, R. L. Ehman, Measurement of normal renal artery blood flow: cine phase-contrast MR imaging vs clearance of p-aminohippurate. *AJR* **161**, 995–1002 (1993).

38. J. F. Debatin, R. H. Ting, H. Wegmuller, F. G. Sommer, J. O. Fredrickson, T. J. Brosnan, B. S. Bowman, B. D. Myers, R. J. Herfkens, N. J. Pelc, Renal artery blood flow: quantitation with phase-contrast MR imaging with and without breath holding. *Radiology* **190**, 371–378 (1994).

39. S. E. Maier, M. B. Scheidegger, K. Liu, E. Schneider, A. Bollinger, P. Boesiger, Renal artery velocity mapping with MR imaging. *J. Magn. Reson. Imaging* **5**, 669–676 (1995).

40. H. G. Bogren, M. H. Buonocore, Blood flow measurements in the aorta and major arteries with MR velocity mapping. *J. Magn. Reson. Imaging* **4**, 119–130 (1994).

41. M. H. Buonocore, Blood flow measurement using variable velocity encoding in the RR interval. *Magn. Reson. Med.* **29**, 790–795 (1993).

42. J. A. Polzin, M. T. Alley, F. R. Korosec, T. M. Grist, Y. Wang, C. A. Mistretta, A complex-difference phase-contrast technique for measurement of volume flow rates. *J. Magn. Reson. Imaging* **5**, 129–137 (1995).

43. C. A. Hamilton, Correction of partial volume inaccuracies in quantitative phase contrast MR angiography. *Magn. Reson. Imaging* **12**, 1127–1130 (1994).

44. D. M. Weber, Y. Wang, F. R. Korosec, C. A. Mistretta, Quantitative velocity images from thick slab 2d phase contrast. *Magn. Reson. Med.* **29**, 216–225 (1993).

45. D. A. Steinman, C. R. Ethier, B. K. Rutt, Combined analysis of spatial and velocity displacement artifacts in phase contrast measurements of complex flows. *J. Magn. Reson. Imaging* **7**, 339–346 (1997).

46. D. N. Ku, C. Zhu, The mechanical environment of the artery, *in* "Hemodynamic Forces and Vascular Cell Biology" (B. E. Sumpio, Ed.), pp. 1–23, Medical Intelligence Unit Book Series 50, R. G. Landes Co., Austin, 1993.

47. R. M. Nerem, Hemodynamics and the vascular endothelium. *J. Biomech. Eng.* **115(4B)**, 510–514 (1993).

48. N. J. Panaro, L. V. McIntire, Flow and shear stress effects on endothelial cell function, *in* "Hemodynamic Forces and Vascular Cell Biology" (B. E. Sumpio, Ed.), pp. 47–66, Medical Intelligence Unit Book Series 50, R. G. Landes Co., Austin, 1993.

49. H. C. Stary, A. B. Chandler, S. Glagov, J. R. Guyton, W. Insull Jr., M. E. Rosenfeld, S. A. Schaffer, C. J. Schwartz, W. D. Wagner, R. W. Wissler, A definition of initial, fatty streak, and intermediate lesions of atherosclerosis: a report from the Committee on Vascular Lesions of the Council on Arteriosclerosis, American Heart Association. *Circulation* **89**, 2462–2478 (1994).

50. J. P. Strong, Atherosclerotic lesions: natural history, risk factors, and topography. *Arch. Pathol. Lab. Med.* **116**, 1268–1275 (1992).

51. R. T. Chalmers, J. J. Hoballah, T. F. Kresowik, W. J. Sharp, A. Y. Synn, E. Miller, J. D. Corson, The impact of color duplex surveillance on the outcome of lower limb bypass with segments of arm veins. *J. Vasc. Surg.* **19**, 279–286 (1994).

52. J. L. Mills, D. F. Bandyk, V. Gahtan, G. E. Esses, The origin of infrainguinal vein graft stenosis: a prospective study based on duplex surveillance. *J. Vasc. Surg.* **21**, 16–22 (1995).

53. K. Okadome, T. Onohara, S. Yamamura, K. Sugimachi, Intraoperative flow waveform analysis aids in preventing early graft failure following reconstruction of arteries of the legs. *Ann. Vasc. Surg.* **5**, 413–418 (1991).

54. H. Nygaard, M. Giersiepen, J. M. Hasenkam, D. Westphal, P. K. Paulsen, H. Reul, Estimation of turbulent shear stresses in pulsatile flow immediately downstream of two artificial aortic valves in vitro. *J. Biomech.* **23**, 1231–1238 (1990).

55. H. Baumgartner, H. Schima, P. Kuhn, Value and limitations of proximal jet dimensions for the quantitation of valvular regurgitation: an in vitro study using Doppler flow imaging. *J. Am. Soc. Echocardiogr.* **4**, 57–66 (1991).

56. M. C. Foshager, D. E. Finlay, D. G. Longley, J. G. Letourneau, Duplex and color Doppler sonography of complications after percutaneous interventional vascular procedures. *Radiographics* **14**, 239–253 (1994).

57. H. S. Bassiouny, S. White, S. Glagov, E. Choi, D. P. Giddens, C. K. Zarins, Anastomotic intimal hyperplasia: mechanical injury or flow induced. *J. Vasc. Surg.* **15**, 708–716 (1992).

58. R. Frayne, B. K. Rutt, Measurement of fluid-shear rate by Fourier-encoded velocity imaging. *Magn. Reson. Med.* **34**, 378–387 (1995).

59. S. E. Maier, H. M. Loree, M. V. McConnell, R. D. Kamm, R. T. Lee, F. A. Jolesz, Computation of blood flow with MR data as boundary condition, *in* "Proc., SMR, 2nd Annual Meeting, San Francisco, 1994," p. 979.

60. J. G. Strang, R. J. Herfkens, N. J. Pelc, Voxel size effects on vascular shear measurement, *in* "Proc., SMR, 2nd Annual Meeting, San Francisco, 1994," p. 1002.

61. S. Oyre, E. M. Pedersen, S. Riggaard, P. Boesiger, W. P. Passke, In-vivo wall shear stress measured by magnetic resonance velocity mapping in the normal human abdominal aorta. *Eur. J. Vasc. Endovasc. Surg.* **13**, 265–271 (1997).

62. Y. Sun, D. O. Hearshen, G. W. Rankin, A. M. Haggar, Comparison of velocity-encoded MR imaging and fluid dynamic modeling of steady and disturbed flow. *J. Magn. Reson. Imaging* **2**, 443–452 (1992).

63. R. Van Type, D. Saloner, L. D. Jou, S. Berger, MR imaging of flow through tortuous vessels: a numerical simulation. *Magn. Reson. Med.* **31**, 184–195 (1994).

64. H. V. Ortega, F. B. Mohamed, M. Godo, S. Vinitski, T. Iwanaga, L. M. Tartaglino, Effect of 3D flow disturbances on MR angiography as studied with 3D computer simulation of blood flow. *Radiology* **201(P)**, 192 (1996).

65. D. A. Steinman, R. Frayne, X. Zhang, B. K. Rutt, C. R. Ethier, MR measurement and numerical simulation of steady flow in an end-to-side anastomosis model. *J. Biomech.* **29**, 537–542 (1996).

66. L. D. Jou, R. van Tyen, S. A. Berger, D. Saloner, Calculation of the magnetization distribution for fluid flow in curved vessels. *Magn. Reson. Med.* **35**, 577–584 (1996).

67. J. M. Tyszka, D. H. Laidlaw, J. M. Silverman, Relative pressure mapping using high-speed three-dimensional phase-contrast cine MRI. *Radiology* **205(P)**, 212 (1997).